Joule

Article

Highly rechargeable aqueous Sn-metal-based hybrid-ion batteries

Highlights

- Silver-coated vertical graphene as a stannophilic host for Sn-metal anode
- Enhanced reversibility and extended lifespan (10,000 h) of the tin anode
- Biphasic electrolyte suppresses Sn^{2+} oxidation
- Aqueous tin-based hybrid-ion batteries without an ion exchange membrane

Authors

Tao Xiao, Lingli Liu, Huan Liu, ..., Haoming Bao, Jin-Lin Yang, Hong Jin Fan

Correspondence

jinlin001@e.ntu.edu.sg (J.-L.Y.), fanhj@ntu.edu.sg (H.J.F.)

In brief

This work presents an effective strategy to enhance the reversibility of tin-based aqueous batteries by integrating a stannophilic porous host with a biphasic electrolyte. A silver-coated vertical graphene (Ag-VG) host significantly enhances the Sn stripping/plating reversibility and material utilization ratio. Biphasic electrolytes allow the construction of a series of tin-anode aqueous full batteries without the employment of ion exchange membranes, showcasing the compatibility of this strategy with different cathode materials. This work provides opportunity to realize long-cycle Sn aqueous batteries.

Xiao et al., 2025, Joule *9*, 101820
March 19, 2025
https://doi.org/10.1016/j.joule.2025.101820

CellPress

Joule

CellPress

Article

Highly rechargeable aqueous Sn-metal-based hybrid-ion batteries

Tao Xiao,[1] Lingli Liu,[1] Huan Liu,[2] Ting Li,[3] Daqian Cai,[1] Wen Siang Lew,[1] Yongqi Zhang,[3] Haoming Bao,[5] Jin-Lin Yang,[1,4,*] and Hong Jin Fan[1,4,6,*]

[1]School of Physical and Mathematical Sciences, Nanyang Technological University, Singapore 637371, Singapore
[2]College of Materials Science and Engineering, Xi'an University of Science and Technology, Xi'an 710054, China
[3]Institute of Fundamental and Frontier Science, University of Electronic Science and Technology of China, Chengdu 611371, China
[4]Energy Research Institute at Nanyang Technological University (ERI@NTU), Singapore 637553, Singapore
[5]School of Chemistry, Chemical Engineering and Biotechnology, Nanyang Technological University, Singapore 637371, Singapore
[6]Lead contact
*Correspondence: jinlin001@e.ntu.edu.sg (J.-L.Y.), fanhj@ntu.edu.sg (H.J.F.)
https://doi.org/10.1016/j.joule.2025.101820

CONTEXT & SCALE Tin (Sn) metal has emerged as a promising candidate for post-lithium multivalent aqueous metal batteries due to its intrinsic resistance to the hydrogen evolution reaction (HER). However, challenges such as uneven Sn deposition and the poor reversibility of the Sn^{2+}/Sn^{4+} reaction severely hinder the development of aqueous Sn-metal batteries. To overcome the first limitation, this work introduces a host material, silver-coated vertical graphene (Ag-VG), which incorporates stannophilic Ag sites within a porous framework. This host enhances the interfacial nucleation kinetics, leading to uniform Sn deposition. For the second challenge, we employ a biphasic H_2O/ionic liquid electrolyte to confine Sn^{2+} within the aqueous phase, avoiding the oxidation of Sn^{2+} and eliminating the need for an ion exchange membrane. Hybrid-ion full batteries without membranes are realized by coupling the Sn-loaded Ag-VG anode and biphasic electrolyte with various types of cathodes, which show relatively high Coulombic efficiency and cycling stability comparable to Zn aqueous batteries.

SUMMARY

Tin (Sn) metal, with its intrinsic resistance to the hydrogen evolution reaction (HER), holds great promise as an anode for safe and rechargeable aqueous Sn-metal batteries (ASBs). However, the major challenges for their practical deployment include uneven Sn deposition and low Sn^{2+}/Sn^{4+} reaction reversibility. To mitigate these challenges, we design ASBs from both anode and electrolyte. First, a stannophilic silver-coated vertical graphene (Ag-VG) host improves the nucleation kinetics and uniform Sn deposition. Second, a biphasic H_2O/ionic liquid (IL) electrolyte confines Sn^{2+} within the aqueous phase, suppressing the formation of Sn^{4+} at the cathode side and eliminating the usage of an ion exchange membrane. The biphasic electrolyte and Ag-VG host are coupled with various types of cathodes (herein, halogens, $LiCoO_2$, and Li_2MnO_4) to fabricate full ASBs. Improved cycling stability and Coulombic efficiency are clearly observed. This work highlights a facile strategy for advancing ASBs.

INTRODUCTION

Owing to the low cost, environmental friendliness, and high safety, rechargeable aqueous batteries have gained attention as promising alternatives to Li-ion batteries for the storage of renewable energy, which avoid the usage of toxic and flammable organic electrolytes. Unfortunately, most of the investigated metal anodes, including Zn, Fe, Mn, In, and Al in neutral or weakly acidic conditions,[1–4] as well as Bi, Cd, and Sb in alkaline systems,[5–7] inevitably suffer from a short cycling life and low Coulombic efficiency (CE) because of the dendrite growth, parasitic byproducts, and hydrogen evolution reactions (HERs).

Among various transition metals, tin (Sn) stands out for its merits of relatively low cost, non-toxicity, and high anti-HER properties.[8] Sn possesses an exceptional hydrogen overpotential and a high redox potential of −0.13 V vs. the standard hydrogen electrode (SHE),[9] implying a low HER tendency and high thermodynamic stability. Moreover, Sn exhibits a body-centered tetragonal crystal structure (I41/amd space group) with relatively minimal surface energy differences between various facets.[10,11] Consequently, Sn metal features an isotropic

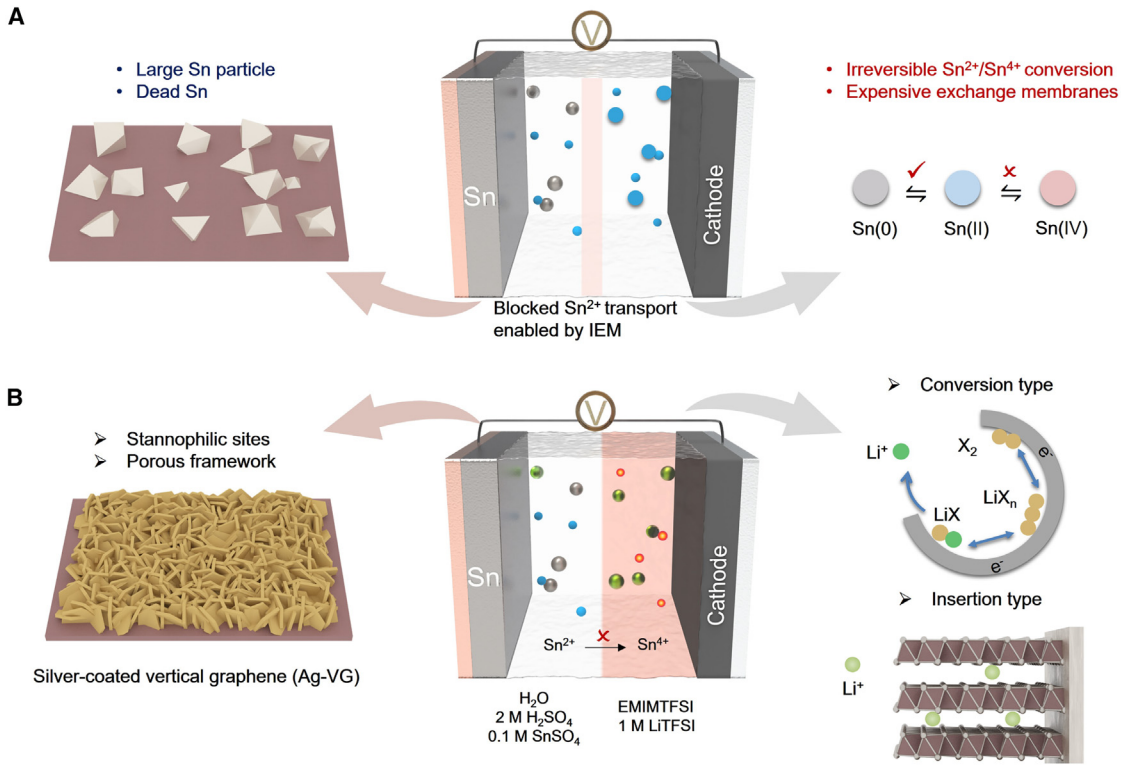

Figure 1. Configuration design for highly reversible aqueous Sn-metal battery

(A) Critical issues in conventional configuration, including uneven deposition due to the large-sized Sn particle and dead Sn, and low reversibility of the Sn^{2+}/Sn^{4+} couple.

(B) Proposed configuration, consisting of stannophilic Ag-VG substrate and biphasic electrolytes of H_2O/ionic liquids.

morphology during electrodeposition, eliminating the needle-like nucleus formation on Li and Zn anodes.[12] Regarding the Sn anode with a conventional configuration (Figure 1A), the deposited polyhedral Sn particles exhibit a dispersed distribution and large sizes and are hard to form into a uniform and compact metallic layer. Furthermore, the large polyhedral Sn particles pose a risk of piercing the separator and are prone to detaching from the substrate and forming "dead Sn," leading to a low CE and shortened cell lifespan. Another critical issue for the Sn anode is the oxidation from Sn^{2+} to inert Sn^{4+} at the cathode side, which leads to serious Sn loss and is detrimental to the cell with a low N/P ratio.[13] These challenges motivate us to design a hybrid-ion battery system for a metal Sn anode.

In recent studies, attention is mainly paid to regulating the Sn deposition behavior by using two main strategies: electrolyte optimization and substrate modification. For the electrolyte strategy, an environment with low water activity, along with the water-deficient Sn^{2+} solvation shell has been shown effective in not only suppressing HER but also promoting a uniform Sn plating process.[14–16] Regarding the substrate modification strategy, copper (Cu) is considered the optimal host or coating material for Sn metal, which acts as a stannophile and hydrogen evolution inhibitor, enabling the Sn anode with high reversibility.[17,18] Despite the improvement in Sn-anode stability in these studies, they generally correspond to a relatively low CE (<99%) and short cycle life (<1,000 h). For the irreversible Sn^{2+}/Sn^{4+} conversion, although a salt bridge can prevent the generation of Sn^{4+} at the cathode, it is certainly not the right choice for practical applications.[19] And the inevitable use of a high-cost ion exchange membrane (IEM) in previous studies is a compromise. Hence, while enhancing the cycle life is an urgent issue for aqueous Sn-metal batteries (ASBs), there is also a pressing need to redesign the battery structure with a low cost.

In this work, we design an ASB to enable ultrahigh Sn anode reversibility and eliminate the usage of IEM. Our key methodology lies in the choice of an aqueous/ionic liquid (IL) biphasic electrolyte and a hierarchical Sn host (Figure 1B). For the biphasic electrolyte, the aqueous acidic $SnSO_4$-based side guarantees the reversible Sn/Sn^{2+} redox pair on the anode, while the IL (EMIMTFSI) part at the cathode side effectively blocks the diffusion of Sn^{2+} and avoids Sn^{4+} formation. To address the issue of the uneven deposition on the anode side, the lightweight and highly conductive graphene-based materials are considered a suitable host for metal deposition, as they can mitigate dendrite growth and buffer volume expansion during plating/stripping.[20] Further, metal species incorporated into carbon hosts can reduce the interfacial energy and suppress HER.[21–23] Hence, in this work, a vertical graphene coated with stannophilic silver-coated vertical graphene (Ag-VG) is employed as the Sn metal host. The VG serves as a porous matrix to lower the nucleation overpotential, and the Ag coating on VG supplies the opulent stannophilic sites, enabling a homogeneous stripping/plating

process with reduced dead Sn. Under an acid condition, the Sn@Ag-VG symmetric cells exhibit a reversible stripping/plating process over 10,000 h at 10% depth of discharge (DOD) and exceeding 3,000 h at 50% DOD. After pairing the Sn@Ag-VG anode with the aqueous/ILs biphasic electrolyte, polyiodide shuttling is overwhelmingly suppressed in an aqueous Sn-I_2 battery, enabling stable cycling for over 2,000 cycles at 1 C (N/P $\sim$ 4.23) with an average efficiency of 99.59%. This IEM-free ASB design has been extended to other intercalation and conversion-type cathodes, including IBr, $LiCoO_2$ (LCO), and Li_2MnO_4 (LMO), showcasing the universality of this strategy in constructing high-performance ASBs.

RESULTS

Sn nucleation and deposition behavior

To maintain low cost and high performance, in this work, Cu and VG are initially selected due to their affordability and stable electrochemical properties, whereas Ag-VG has been designed for further performance optimization due to the stannophilic nature of Ag. The fabrication and characterization of the Ag-VG and VG can be found in the methods, Figure S1, and Note S1. The electrochemical properties of the substrates were first investigated in the electrolyte containing 2 M H_2SO_4 + 0.1 M $SnSO_4$. Tafel plots were conducted to evaluate the anti-corrosion performance (Figure S2A). The Ag-VG exhibits a reduced exchange current density (2.52 mA cm^{-2}) compared with Cu (12.44 mA cm^{-2}) and VG (8.89 mA cm^{-2}). Regarding HER activity, Ag-VG exhibits a lower H_2 evolution potential (Figure S2B), signifying a suppressed HER tendency. Furthermore, the nucleation-growth behavior of Sn on different substrates was analyzed by chronoamperometry (CA) measurements. The CA test was conducted at varying overpotentials relative to the open-circuit potential (OCP) to compare the nucleation behavior on three hosts (Figure S3). The resulting data were normalized to $(I/I_m)^2$-(t/t_m) curves and analyzed using the Scharifker-Hills model,[24] which includes four nucleation models: 2D progressive (2DP), 2D instantaneous (2DI), 3D instantaneous (3DI), and 3D progressive nucleation (3DP). Generally, instantaneous nucleation corresponds to rapid nucleation where all nucleation sites are occupied at the initial stage, while progressive nucleation exhibits slower nucleation kinetics, with nucleation sites being gradually occupied over time.[25] The CA test results indicate that the dimensionless curves of Sn plating on all substrates align perfectly with the 3DI model (Figures 2A and S4), suggesting that the nucleation is rapidly completed during the initial Sn plating. This finding is consistent with the results of cyclic voltammetry (CV) tests conducted under a three-electrode configuration. For the Cu substrate, a nucleation loop appears in the first cycle but disappears in the second, indicating no further nucleation in subsequent growth, while for Ag-VG and VG, the absence of a nucleation loop in the first cycle suggests an ultralow nucleation overpotential (Figures S5 and S6). Further, based on the 3DI model, the nuclei density, nuclei radius, and diffusion coefficient of three substrates at varying overpotentials can be obtained[26] (Figures 2B and S7). Ag-VG consistently exhibits the richest nuclei density and the most refined nuclei size compared with Cu and VG across all potentials. Additionally, Ag-VG has the lowest diffusion coefficient, indicating a high barrier for Sn^{2+} migration. These fitted results can be attributed to disparities in Sn^{2+} adsorption characteristics and nucleation barriers across different substrates. Galvanostatic voltage profiles reveal that both Ag-VG and VG exhibit much reduced nucleation overpotentials compared with Cu (Figure 2C). Additionally, according to density functional theory (DFT) calculations (Figure S8), the adsorption energy of the Sn^{2+} on graphene (002) is -0.19 eV, which is quite small and suggests weak interaction and fast diffusion of Sn^{2+} on graphene (002). As a comparison, amorphous Ag and Cu (220) display enhanced adsorption energies, reflecting the stannophilic nature of Ag-VG and Cu hosts. Benefiting from the combination of strong Sn^{2+} affinity and reduced nucleation barrier, Ag-VG exhibits optimized nucleation behaviors. According to the Arrhenius plot derived from electrochemical impedance spectroscopy (EIS) at various temperatures (Figure S9), the introduction of a nuclei-rich host effectively reduces the electroplating activation energy.

To investigate the influence of nucleation mechanisms on Sn deposition behavior, we first monitor the deposition morphology evolution on three substrates. Under low areal capacity conditions of 0.1 mAh cm^{-2}, the scanning electron microscopy (SEM) image of Sn@Ag-VG reveals more uniformly distributed and smaller Sn particles (Figure 2D). In contrast, Sn@Cu and Sn@VG exhibit larger particles with a noticeably random and uneven distribution (Figures 2E and 2F). As the deposition capacity increases to 10 mAh cm^{-2}, Sn@Ag-VG shows a compact and flat surface morphology (Figure 2G), in contrast to the evident cracks and irregularities observed in the Sn@Cu and Sn@VG (Figures 2H and 2I). This morphological difference is consistently observed across varying current densities (Figure S10). The compactness of the deposition on Ag-VG can also be inferred from the X-ray diffraction (XRD) patterns (Figure S11). Confocal laser scanning microscopy (CLSM) characterization reveals that, compared with the smooth morphology observed on Ag-VG, both Cu and VG exhibit relatively rough and fluctuated contours. Corresponding surface roughness analysis reveals that the S_a (arithmetical mean height) and S_z (maximum height) values of the Ag-VG are both much lower than those of Cu and VG, suggesting more homogeneous deposition behavior (Figure S12). The reduced height fluctuations on the Ag-VG further validate the suppression of rampant Sn particle growth (Figure S13). The uneven Sn nucleation and growth behaviors on Cu and VG lead to whisker structure and large aggregates, respectively (Figures 2J–2L, S14, and S15; Note S2), compared with the uniform deposition on Ag-VG. The optimized Sn deposition behavior on Ag-VG is more evident from the morphological evolution at low areal capacities (Figure S16). It is observed that Sn particles initially arrange along the contour of the top surface of VG. As deposition progresses, these particles aggregate to form an island-like morphology. This preferential deposition is attributed to the difference between the graphene sidewalls and edges in their reactivity and adsorption capability. In contrast, large-scale uniform Sn particles are observed on the Ag-VG. At low areal capacities, the presence of uniformly distributed stannophilic Ag sites facilitates the deposition of high-density Sn on both the top and sides of the Ag-VG. As the areal capacity increases, Sn particles progressively fill the 3D framework

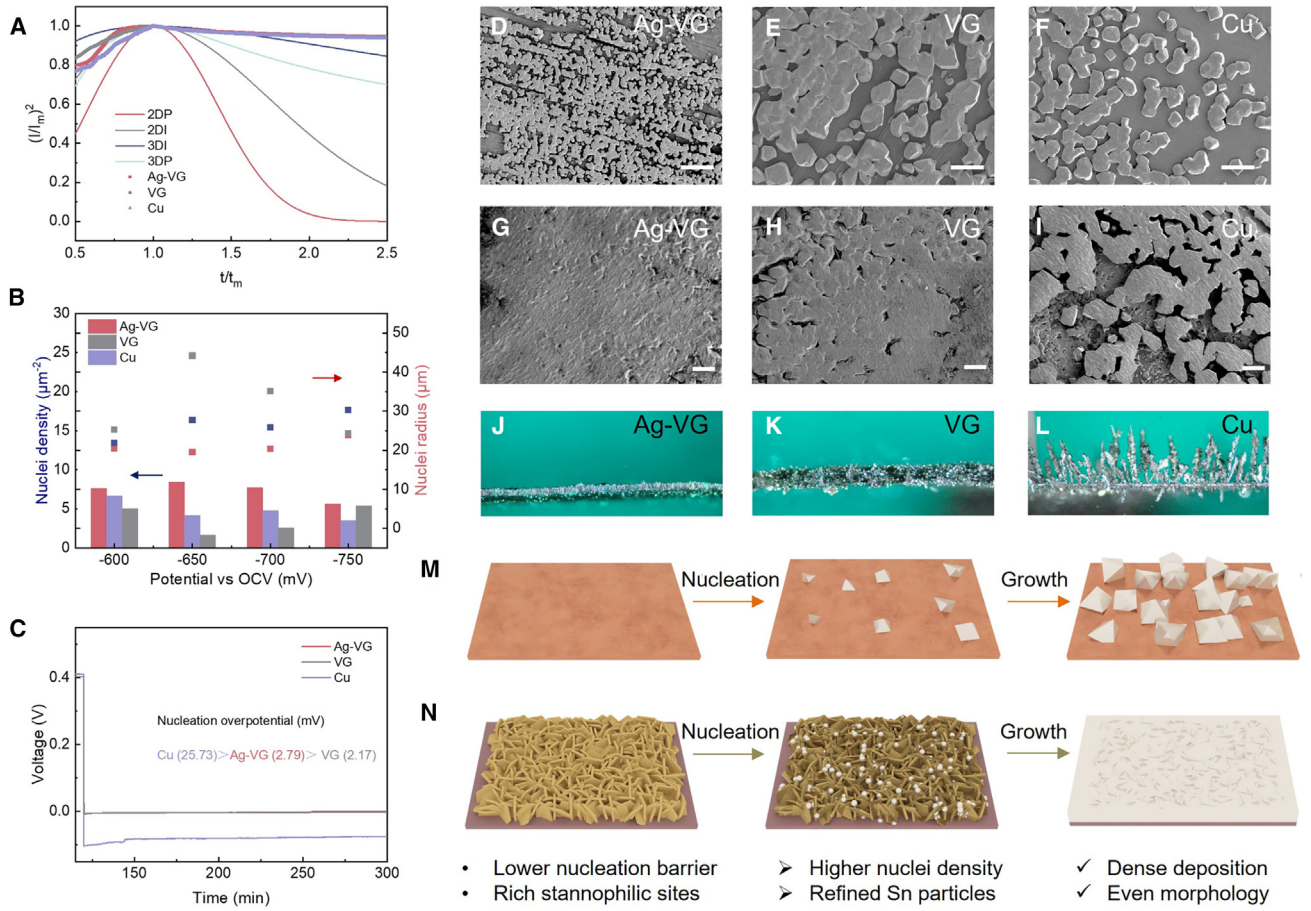

Figure 2. Sn electrochemical and deposition behaviors on three substrates

(A) $(I/I_m)^2$-(t/t_m) curves derived from the chronoamperometry test of three substrates (Cu, VG, and Ag-VG), and theoretical instantaneous and progressive nucleation profiles described in the Scharifker-Hills model (2DP, 2DI, 3DI, and 3DP).

(B) Nuclei density and radius of plated Sn on three substrates at varying overpotentials. The histogram and scatter plot refer to nuclei density and radius, respectively.

(C) Galvanostatic discharge curves of Sn-substrate half-cells of Cu, VG, and Ag-VG.

(D–I) SEM images of Ag-VG, VG, and Cu after deposition at varying areal capacity. The deposition parameters are 0.1 mA cm^{-2} and 1 mAh cm^{-2} for (D)–(F) and 1 mA cm^{-2} and 10 mAh cm^{-2} for (G)–(I). The scale bars are 2 μm for (D)–(F) and 100 μm for (G)–(I).

(J–L) *In situ* optical microscopy images of (J) Ag-VG, (K) VG, and (L) Cu after 20 min deposition at a current density of 5 mA cm^{-2}.

(M and N) Proposed Sn-metal deposition mechanism on (M) Cu and (N) Ag-VG host.

of Ag-VG, eventually covering its entire surface. These observations (Figure S16) highlight the effectiveness of Ag-VG that combines stannophilic sites with a 3D porous VG framework in promoting uniform Sn deposition. However, the effect cannot be replicated by replacing Ag with Cu, despite that Cu also can induce a stannophilic surface. This is attributed to their difference in electronegativity and anti-HER capabilities, underscoring the critical role of Ag in this host design (Figure S17 and Note S3).

Based on the analysis of the nucleation model and morphology characterization, the deposition mechanism of Sn metal on three substrates is proposed (see schematics in Figures 2M and 2N). Since Sn nucleation on three substrates adheres to the 3DI model, the nucleation stage primarily determines the subsequent growth and final deposition morphology. For the Cu substrate, the relatively low fraction of Sn nucleates due to the high nucleation barrier leads to large-sized Sn particles and uneven deposition. Meanwhile, the high diffusion coefficient facilitates the migration of Sn^{2+} and exacerbates the evolution of protrusions. This nucleation mechanism can also be reflected by the simulation of the Sn^{2+} concentration gradient and the local current density (Figures S18 and S19). Although VG exhibits the lowest nuclei density, the lower migration barrier for Sn^{2+} hinders substantial ion accumulation on the surface during deposition, thereby mitigating the uneven distribution of Sn^{2+} relative to Cu. In contrast, the enriched nucleation sites and uniform Sn^{2+} adsorption on the Ag-VG result in a minimal ion concentration gradient and the lowest local current density. This promotes the formation of finer Sn particles and dense deposition.

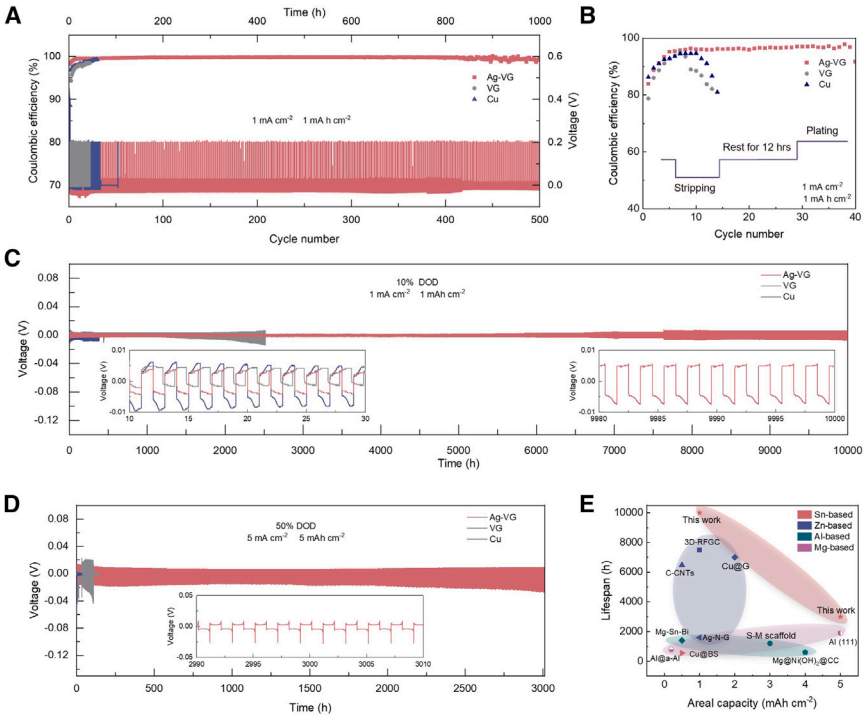

Figure 3. Reversibility evaluation of Sn-metal deposition on various substrates

(A) Sn plating/stripping behavior on three substrates at an areal capacity of 1 mAh cm^{-2}.

(B) Calendar life test of Sn-substrate half-cells at an aging period of 12 h.

(C) and (D) Cycling performance of Sn@substrate symmetric cells at two DOD conditions.

(E) Performance comparison between this work and other relevant reported work in aqueous metal-ion batteries.

Reversibility evaluation of the Sn metal

After the Sn deposition behavior is optimized by designing the Ag-VG host, the reversibility of Sn metal is initially assessed through a cyclic stripping/plating process on various substrates. The CE of Sn-substrate half-cells was measured and employed as a critical indicator of reversibility. For VG and Cu substrates, the CE begins to fluctuate violently within the first 50 cycles, ultimately achieving average values of 96.71% and 97.02%, respectively (Figure 3A). In stark contrast, the Ag-VG half-cell retains stable cycling with an average CE of 99.72% over 1,000 h. In the calendar life test, Ag-VG exhibits relatively stable cycling and prolonged cycle life compared with the other substrates at an aging time of 12 h, resulting in an average CE of 90.17% over 20 days (Figure 3B). In comparison, VG and Cu showcase an obvious drop in CE within fewer than 10 cycles, indicating severe degradation of the host under static conditions.

Reversibility evaluations were conducted on symmetric cells at varying current densities and DOD conditions. Before assembling symmetric cells, all three substrates were initially pre-deposited with Sn metal of 10 mAh cm^{-2}. The symmetric cells with bare Sn plates experienced rapid short-circuiting within 200 h under both 10% and 50% DOD conditions, suggesting the severe degradation of Sn metal due to the presence of large Sn particles and dead Sn (Figure S20). Among the various Sn-metal hosts, the Ag-VG symmetric cell demonstrates stable short-circuit-free cycling at 10% DOD conditions of over 10,000 h, which is far superior to VG or Cu at the areal capacity of 1 mAh cm^{-2} (Figure 3C). Correspondingly, the enhanced reversibility can be reflected by the post-cycling morphology evolution (Figure S21). Unlike the discontinuous and rough surfaces observed on VG and Cu, Ag-VG displays a compact and flat deposited surface. Even at a considerable plating areal capacity of 5 mAh cm^{-2} and 50% DOD conditions, Ag-VG still displays noticeable durability over 3,000 h with a minimal polarization of 25 mV (Figure 3D). This performance far surpasses that of most other relevant works in aqueous metal-ion batteries summarized in Figure 3E,[18,20,27–34] underscoring the crucial role of Ag-VG in enhancing the reversibility of Sn metal. In addition, the performance of symmetric cells under 80% DOD corroborates the effectiveness of Ag-VG under extreme conditions (Figure S22).

Active phase separation and Sn^{2+} confinement enabled by BPE

The Sn^{2+} oxidation in ASBs with a conventional single-phasic configuration is a primary factor contributing to low reversibility. To address this issue, IL EMIMTFSI with considerable hydrophobicity and ionic conductivity were utilized to impede the electromigration and diffusion of Sn^{2+}. Due to the difference in polarity, H_2O/ILs can act as immiscible solvent pairs and form a stable phase interface through active phase separation, which can rapidly recover even after severe external disturbances (Figure 4A). The rapid and stable phase separation between these two liquid phases is also clearly illustrated by molecular dynamics (MD) simulations (Figure S23). This finding is further supported by the simulated density profile of H_2O, where water molecules are notably concentrated in the middle region represented by the aqueous phase. These simulation results can be further corroborated by the characterization of ^1H nuclear magnetic resonance (NMR) and Raman spectra. Raman spectroscopy in Figure 4B displays that the characteristic vibrational band of O–H belongs to H_2O in the top phase, while the distinct characteristic peaks including C–H and N–H from the imidazole ring in $EMIM^+$ appear only for the bottom phase, signifying the IL-rich bottom phase and the H_2O-dominated top phase. These signals are also consistent with the ^1H NMR spectra of the two phases, where the absence of the H_2O signal (around 4.74 ppm) in the IL phase can be observed (Figure S24A).

Furthermore, the distribution of the main ions in the biphasic electrolyte along the phases interface under static conditions

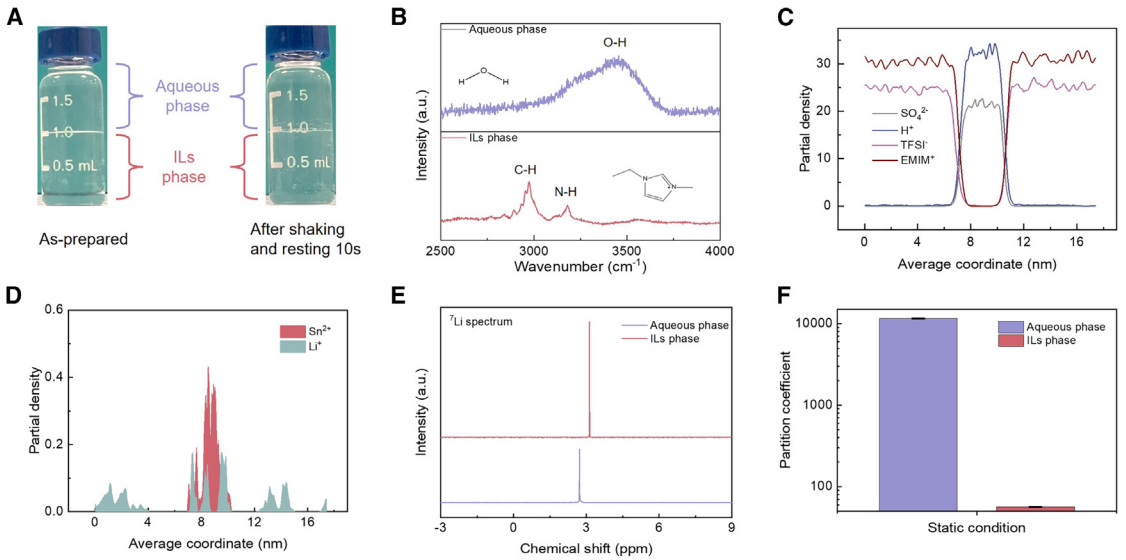

Figure 4. Phase separation and Sn^{2+} localization enabled by ILs/H_2O biphasic system

(A) Photograph of active phase separation between the ionic liquids EMIMTFSI and water.

(B) Raman spectra of two separated phases under static conditions.

(C) MD simulation results of the distribution of major ions of biphasic electrolyte along the phase interface under static conditions. 7–11 nm corresponds to the water phase region.

(D) Simulated distribution of Li^+ and Sn^{2+}.

(E) ^{7}Li NMR characterization of water phase and IL phase.

(F) ICP-OES results of Sn^{2+} distributed in aqueous phases and IL phase under static conditions after 1 week. Error bars show the range of variation for triple measurements, and the data points with error bars represent the mean ± standard deviation.

was also simulated by the MD method. The water phase is primarily dominated by H^+ and SO_4^{2-}, while the IL phase is predominantly occupied by $EMIM^+$ and $TFSI^-$ (Figure 4C). Li^+ exhibits a comparable partial density distribution in both the ILs and water phases, implying that Li^+ can function as a mediator ion across both phases (Figure 4D). This simulation result can be confirmed by the evident peak signals observed in the ^{7}Li NMR spectra in both the top and bottom phases (Figure 4E). Considering the relatively poor transport capability and solubility of $TFSI^-$ within the biphasic system, despite the fact that the ^{9}F NMR spectrum indicates a distinguished F signal detected in both phases (Figure S24B), Li^+ can be viewed as the dominant mediator ion. The partial density of Sn^{2+} exhibits a pronounced concentration in the central region, suggesting that it is fully localized within the aqueous phase. Subsequently, ICP-OES was employed to quantify the Sn^{2+} distribution in the top and bottom phases (Figure 4F). The ICP-OES results reveal a partition coefficient of 11,585 in the water phase and 57 in the IL phase, ultimately enabling a high Sn^{2+} concentration ratio of about 205 between the two phases. Hence, it has been shown that the ILs and water can achieve a stable phase separation, with Sn^{2+} being nearly fully confined to the aqueous phase.

Electrochemical performance and reaction mechanism of aqueous Sn-I_2 battery

Full cells are fabricated to validate the effectiveness of Ag-VG host and biphasic systems in ASBs. To couple with the Sn-metal anode, a conversion-type cathode based on an I^-/I^0 redox couple was first employed owing to its relatively high specific capacity (211 mAh g^{-1}) and discharge plateau (0.54 V vs. SHE). The electrochemical performance of Sn-I_2 batteries was evaluated in both a single-phasic electrolyte (SPE) and biphasic electrolyte (BPE) (Figure 5A). In the CV curve of an SPE battery, three distinct oxidation peaks and two relatively weak reduction peaks are observed. Such an asymmetric electrochemical process indicates relatively poor reversibility, primarily due to the oxidation of Sn^{2+}. In contrast, the CV profile of a BPE battery shows only one reversible redox couple. The proposed reaction mechanisms of the Sn-I_2 batteries with BPE and SPE systems are illustrated in Figure 5B. Regarding the SPE battery, taking the charging process as an example, the reaction primarily involves the conversion of Sn^{2+}/Sn^{4+} and SnI_2/SnI_4. Due to the thermodynamic unfavorability and the low solubility of SnI_2 and SnI_4, these conversions are kinetically sluggish and not fully reversible. The reaction path in BPE consists of a stripping/plating process on the anode side and the conversion of iodine species on the cathode side. In the BPE system, the Sn^{2+} is supposedly confined within the H_2O phase and cannot migrate to the iodine side for further oxidation, while the Li^+ serves as the mediating ion shuttling between the two phases to maintain charge balance during the charge and discharge process. The disparity of reaction path and reversibility between BPE and SPE is also reflected in the galvanostatic voltage profiles of corresponding full cells (Figure 5C). For the SPE battery, the reduced discharge capacity leads to a low CE of 57.5%. As a comparison, the BPE Sn-I_2 battery gives a higher CE of 98.1%, highlighting the enhanced reversibility. To gain further insight into the reaction process of a BPE battery, X-ray photoelectron spectroscopy (XPS) was

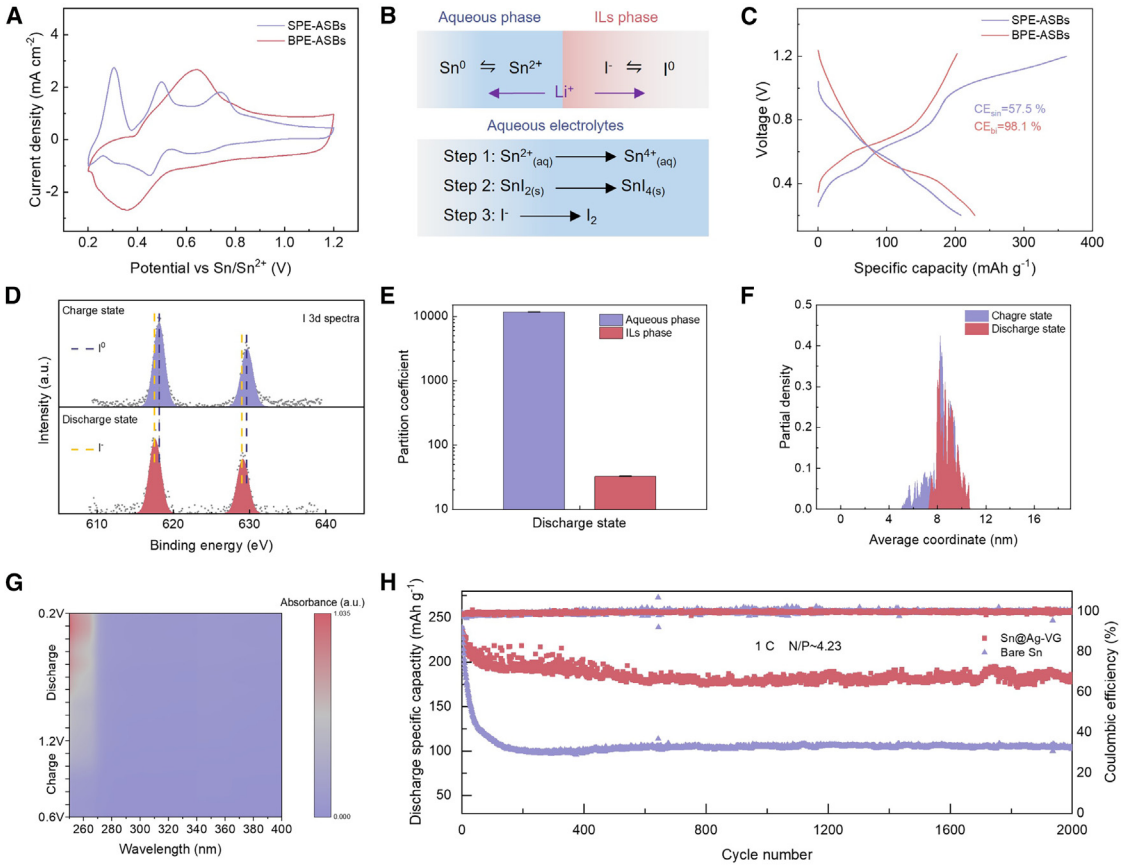

Figure 5. Electrochemical behavior and full cell performance of an aqueous Sn-I_2 battery

(A) CV profiles of aqueous Sn-I_2 batteries based on single-phasic and biphasic electrolytes (SPE and BPE).

(B) Illustration of the proposed reaction path of the full cells with SPE or BPE.

(C) Galvanostatic charge-discharge (GCD) curves of Sn-I_2 batteries based on SPE and BPE in the first cycle.

(D) *Ex situ* XPS analysis for the I 3d spectrum of cathodes after charging and discharging.

(E) ICP-OES results of Sn^{2+} distributed in aqueous phases and IL phase after discharging. Error bars show the range of variation for triple measurements, and the data points with error bars represent the mean ± standard deviation.

(F) Simulated Sn^{2+} distribution across the phase interface at charge and discharge states. 7–11 nm represents the water phase region.

(G) *In situ* UV-vis spectra of aqueous phase in Sn-I_2 batteries during the charging and discharging process.

(H) Cycling performance of Sn-I_2 batteries at 1 C (1 C = 211 mAh g^{-1}).

implemented to reveal the valence evolution of Sn and I species at discharge and charge states (Figure 5D). High-resolution I 3d spectral peaks of the cathodes after charge locate at 630.4 and 618.3 eV, verifying the presence of I_2 molecules. After full discharge to 0.2 V, the two characteristic I 3d peaks shift negatively to 629.1 and 617.4 eV, corresponding to the reduction of I_2 molecules to a low-valent state (I^-) due to the generation of LiI. For the Sn anodes, the high-resolution Sn 3d spectrum consistently showcases a single pair of peaks, implying the elimination of the Sn^{4+}. Moreover, the slight positive shift of the Sn 3d peak in the charge state originates from the electron transfer between Sn and Ag due to interfacial alloying, which will benefit the lifespan of Sn metal[35–37] (Figure S25).

To verify the confinement of Sn^{2+} in the water phase, ICP-OES was employed to quantify the concentration of equilibrated Sn^{2+} in each phase after discharge (Figure 5E). The concentrations of Sn^{2+} in the aqueous phase and IL phase are 11.17 and 0.03 mg mL^{-1}, respectively. While the majority of Sn^{2+} is localized in the water phase, the slightly increased partial coefficient of Sn^{2+} in the H_2O phase compared with that of static conditions can be attributed to the oxidation of Sn metal during the discharge process. Additionally, the CV curve of the Sn||Carbon paper half-cell with SPE exhibits a distinct oxidation peak corresponding to the Sn^{2+}/Sn^{4+} redox couple (Figure S26A). In contrast, there are no obvious characteristic peaks throughout 50 cycles in BPE (Figure S26B), indicating the suppressed electromigration of Sn^{2+} toward the cathode in BPE. MD simulations also show that, regardless of the charge and discharge states, the Sn^{2+} consistently displays a major density distribution in the aqueous region, suggesting the localization of Sn^{2+} on the anode side (Figure 5F), and the simulated H_2O molecules are always mainly distributed in the initial aqueous area (Figure S27).

Given the typical shuttle effect in aqueous iodine batteries, the evolution and shuttle behavior of polyiodides were studied under

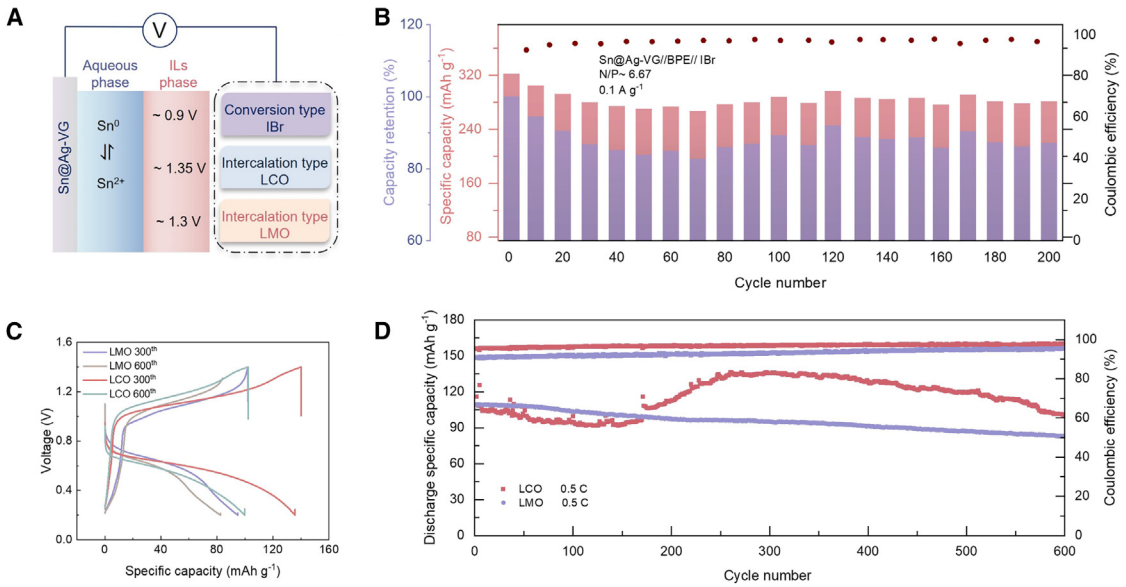

Figure 6. Exchange membrane-free ASBs with other cathode materials

(A) Schematics of membrane-free ASBs based on Ag-VG host and various cathodes including IBr, LCO, and LMO. Voltage refers to the equilibrium potential of the corresponding assembled full cell.

(B) Cycling stability of Sn@Ag-VG//BPE//IBr battery under 0.1 A g^{-1}.

(C) GCD profile of ASBs based on LCO and LMO.

(D) Long-term cycling performance of full cells with intercalation cathode at 0.5 C (LCO:1 C = 274 mAh g^{-1}; LMO:1 C = 148 mAh g^{-1}).

static conditions. Pre-configured polyiodides were dissolved in the IL phase, forming a biphasic system with the aqueous solution. After 1 week, no color change was observed in the upper aqueous phase. The corresponding UV-vis spectrum confirms the absence of polyiodide signals, indicating that the IL phase effectively prevents polyiodide shuttling (Figure S28). Next, the evolution of polyiodide species during the charge and discharge process was monitored by *in situ* UV-vis spectroscopy. For the SPE system, due to the low solubility of SnI_2/SnI_4 in aqueous solutions, orange particles can be observed during the charging process, consistent with the CV profiles in Figure 5A. In contrast, the generated polyiodides are mainly confined to the bottom IL phase (Figure S29). Correspondingly, the *in situ* UV-vis spectrum displays the absence of two typical absorption peaks (around 288 and 350 nm) of I_3- in the H_2O phase throughout the entire process (Figure 5G), implying the strong inhibition of polyiodide shuttling toward the Sn anode by the biphasic system. This phenomenon can be attributed to the strong affinity of $EMIM^+$ with polyiodide ions, which has also been observed and confirmed in zinc-iodine batteries.[38]

Our BPE design enables an aqueous Sn–I_2 full cell with high reversibility upon long cycles, and the highly conductive Ag-VG host will also benefit from the kinetic performance. We compare the BPE-based Sn-I_2 battery by using bare Sn plate and Sn@Ag-VG. The latter exhibits a reduced voltage difference between the two redox peaks and a higher current peak in the CV curve (Figure S30A), suggesting an improved ion transfer and enhanced interfacial kinetics. Additionally, the full cell with Sn@Ag-VG delivers average capacities of 197.4, 176.1, 150.8, 139.4, and 117.3 mAh g^{-1} at rates from 1 to 20 C (Figure S30B), consistently outperforming the full cell assembled with bare Sn plate. Beyond the enhancement in rate capability, the long-term cycle stability is also evidently optimized with the incorporation of the Ag-VG host (Figure 5H). The full cell assembled with bare Sn exhibits a CE of 99.50%, with the discharge-specific capacity declining from 238.91 to 103.82 mAh g^{-1}, resulting in a capacity retention of 43.45%. In contrast, the full cell with Ag-VG at a low N/P ratio of 4.23 demonstrates a discharge-specific capacity of 179.24 mAh g^{-1} and average CE of 99.59% after 2,000 cycles. The superior cycle stability is also observed under high current conditions of 10 C (Figure S31).

ASBs with other cathodes

To further demonstrate the potential of ASBs based on our Ag-VG and biphasic systems for energy storage applications, we expand to other types of cathode materials with different mechanisms and redox potentials (Figure 6A), including iodine bromide (IBr), lithium cobalt oxide (LCO), and lithium manganese oxide (LMO). IBr is a conversion-type cathode. Compared with iodine, the solid interhalogen compound IBr enhances the discharge platform and specific capacity, with oxidized Br^0 anchored by iodine to prevent the generation and shuttling of Br_2/Br_3^-.[39] As the conversion reactions involve multiple halogens, the CV profile of a Sn@Ag-VG//BPE//IBr full cell exhibits multiple distinct redox peaks, attributed to two primary redox couples of I^-/I^0 and IBr/Br^- (Figure S32). The corresponding full battery delivers a specific capacity of 281.1 mAh g^{-1} and a capacity retention rate of 87.16% after 200 cycles at 0.1 A g^{-1} with an N/P ratio of 6.67, along with an average CE of 96.83% (Figure 6B). LCO and LMO are two typical intercalation cathode

materials. The full cells assembled with these two cathodes consistently displayed clear voltage transition platforms in the GCD curves (Figure 6C), corresponding to the insertion and extraction of lithium ions. These cells show a reasonable capacity retention after 600 cycles at 0.5 C (Figure 6D).

DISCUSSION

Developing metal anodes with robust resistance to HER and dendrite growth is highly necessary for the commercialization of low-cost, high-safety rechargeable metal aqueous batteries, contributing to the sustainability of the global energy supply. Compared with the intensively studied Zn metal, Sn metal has emerged as a promising anode material in aqueous batteries due to its exceptional corrosion resistance. However, the challenges lie in the non-uniform deposition of Sn metal and the low reversibility of the Sn^{2+}/Sn^{4+} redox couple. In this work, we have achieved a Sn-metal anode with ultrahigh reversibility and exchange membrane-free Sn-metal batteries with high CE under high Sn-metal utilization. This achievement is attributed to the synergistic effects of a biphasic electrolyte composed of H_2O/ILs and a stannophilic porous Ag-VG host. The biphasic system effectively confines Sn^{2+} to the aqueous phase, thus mitigating the challenges posed by the Sn^{2+}/Sn^{4+} couple. The Ag-VG host establishes a densely nucleated interface, enhancing the grain refinement and enabling an exceptional lifespan under a DOD of up to 80%. To prove the universal validity of this protocol, a series of practical ASB prototypes have been fabricated, in which the highly reversible Sn-metal anode is coupled with various cathode materials (conversion and intercalation-types). These full batteries exhibit energy densities comparable to other reported aqueous acid batteries (Tables S1 and S2). These findings provide a crucial foundation for future research into durable, eco-friendly energy storage solutions, promoting the commercialization of sustainable metal aqueous batteries.

METHODS

Fabrication of VG and Ag-VG

To fabricate the VG, typically, a 6 × 6 cm^2 Cu foil was placed in the chamber of a plasma-enhanced chemical vapor deposition (PECVD) device and then introduced into a mixed atmosphere of methane:hydrogen:argon = 6:10:20 sccm. The chamber was then heated to 500°C at a rate of 10°C min^{-1} and treated at a power of 500 W for 8 min. Finally, it was cooled to room temperature (RT) and the sample was taken out. To fabricate the Ag-VG, the Ag deposition was conducted in an AJA International ATC-Orion 8-target UHV magnetron sputtering deposition system with a 2-in. Ag target. The sputtering was conducted at RT under a pressure of 2 mTorr and a power of 50 W.

Preparations of electrodes and electrolytes

For full cells with BPE, the glass fiber filters (GF-D 1825, Whatman) and hydrophilic PP separator were employed as the separators toward the anode side and cathode side, respectively. 50 μL of 2 M H_2SO_4 + 0.1 M $SnSO_4$ and 50 μL of 1 M LiTFSI + EMIMTFSI were used as the electrolytes for the anode side and cathode side, respectively.

For the halide cathodes, in a typical fabrication process, 320 mg of activated carbon and 40 mg of super P were dissolved in 1.5 mL of NMP with polyvinylidene fluoride (PVDF) (2.5 wt %) and stirred for 4 h. Then, the slurry was pasted on the hydrophilic carbon paper with an area of 3 × 3 cm^2 and dried at 65°C in an electric oven overnight. Finally, the ethanol solution of LiI or IBr was slowly dripped on the obtained carbon substrate and finally vacuum dried. The areal mass loadings of LiI or IBr was about 5 mg cm^{-2}, and their specific capacities are calculated based on the mass of iodine and IBr, respectively. For the LCO and LMO, the cathode slurry for the full cell was fabricated by mixing commercial cathode materials, super P (10 wt %), and PVDF binder with the ratio of 8:1:1 in NMP to form a homogeneous slurry. The obtained slurry was uniformly coated on the Ti foil through the doctor-blade method. The areal mass loading was 0.8–1.1 mg cm^{-2}.

Materials characterization

The thickness of the film was determined using an atomic force microscope (Park System NX10). The field emission scanning electron microscopy (SEM, ZEISS SUORA®55) with an energy dispersive spectrometer (EDS) was used to collect the SEM image and mapping results of the sample. The X-ray photoelectron spectra profile was obtained using an X-ray photoelectron spectrometer (XPS Kratos AXIS Supra). A 400 MHz Nuclear Magnetic Resonance Spectroscope (JEOL ECA400, Tokyo, Japan) was employed to collect the ^1H, ^7Li, and ^9F spectra of the liquid sample. The XRD patterns were characterized by Bruker D8 Advance (Cu Kα, λ = 0.15418 nm). *In situ* deposition images of different substrates were obtained by *in situ* optical microscopy. The UV-vis spectral results of samples were obtained using a UV-vis spectrophotometer (UV-1900, Shimadzu). Raman spectrometers (Horiba LabRAM HR Evolution) were employed to obtain the Raman signal of the C–H or –OH vibrational band in different phases. ICP-OES results were obtained using a Varian Agilent 720ES spectrometer. Laser confocal scanning microscopy (LCSM) images of the various substrates after deposition were attained using a laser microscope (Olympus LEXT OLS5000). The surface roughness can be calculated based on the equation below, where S_a represents the average height, S_z represents the peak height, and A denotes the tested area.

$$S_a = A^{-1}\left[\iint_A |Z(x,y)|dxdy\right]$$

Electrochemical measurements

Symmetric cells, half-cells, and various full cells were assembled in the form of CR2032 coin cells. All the cells mentioned above were tested on a LAND battery testing system (CT3002AU, China). The CV curves, Tafel plots, LSV curves, and EIS data were all collected using a CHI760D electrochemical workstation. The CA test was completed by the CA module in the Autolab workstation with a sampling time of 0.004 s. Tafel profiles were measured between −0.16 and 0.16 V using the symmetric cells of Sn@substrate electrodes. All substrates were pre-deposited with Sn metal with an areal capacity of 10 mAh cm^{-2}. A three-electrode

configuration was employed, with a Sn plate as the counter electrode, the substrate as the working electrode, and SCE as the reference electrode, to assess HER activity and obtain the CV curves for Sn deposition-dissolution. HER was evaluated using the LSV method over a scan range of −0.4 to −1 V on various substrates. The Sn deposition-dissolution curves were recorded by the CV method over a scan range of −0.2 to −0.6 V. The corrosion current density was determined from the software in CHI760D. EIS measurements were conducted at a constant amplitude of 5 mV over a frequency range from 1 Hz to 100 kHz.

Nucleation parameter calculations

For the instantaneous nucleation model, the Sn^{2+} diffusion coefficient (D), nuclei density (N), and nuclei radius (r) can be calculated with the following equations.

$$N = \frac{{I_m}^2}{0.41 k_i z^2 F^2 D^2 c^2}$$

$$k_i = \sqrt{\left(\frac{8\pi c M}{\rho}\right)}$$

$$D = \frac{{I_m}^2 t_m}{0.1629\left(z^2 F^2 c^2\right)}$$

$$r = \sqrt{\left(\frac{1}{\pi N}\right)}$$

where I_m and t_m are the maximum current density and its corresponding time in the $(I/I_m)^2 - t/t_m$ dimensionless curves, M is the molar weight of the Sn deposit (g mol^{-1}), ρ is the density of the Sn metal (g cm^{-3}), c is the Sn^{2+} concentration (mol cm^{-3}), z is the number of electrons involved in the deposition process, and F is the Faraday constant.

Theoretical calculations

To simulate the deposition and distribution of ions on different electrode surfaces, finite element simulation of the deposition process was conducted using COMSOL Multiphysics. The modules used include electrochemistry and transport of diluted species. The governing equations for the electrochemistry module are as follows:

$$\nabla \cdot i_l = Q_l, i_l = -\sigma_l \nabla \phi_l$$

$$\nabla \cdot i_s = Q_s, i_s = -\sigma_s \nabla \phi_s$$

Here, ϕ_l is the electrolyte potential, ϕ_s is the potential, σ_l is the electrolyte conductivity, σ_s is the electrode conductivity, i_l is the electrolyte current, and i_s is the electrode current. The diffusion behavior of the electrolyte is solved using the transport of diluted species module, with its governing equation being the following:

$$\nabla \cdot J_i + u \cdot \nabla c_i = R_i$$

Since the electrolyte flow velocity is approximately zero, the governing equation can be simplified as follows:

$$\nabla \cdot J_i = R_i, J_i = -D_i \nabla c_i - z_i u_{m,i} F c_i \nabla V$$

Here, D_i is the diffusion coefficient, Z_i is the electrolyte charge, $u_{m,i}$ is the mobility, F is the Faraday constant, c_i is the concentration, and V is the potential. To ensure the accuracy of the simulation, the densest conventional triangular meshes are used for all simulations under the MUMPS solver.

MD simulation: the MD were performed using the software package GROMACS (version 2021.3).[40,41] The molecules were optimized in ORCA first. The system was constructed by packmol.[42] The atomic interactions were parameterized by the optimized potentials for liquid simulations all-atom (OPLS-AA) force field,[43] and RESP2 charge obtained from Multiwfn[44] was applied in the calculations. After the energy minimization, the systems were pre-balanced in NPT ensemble with the Berendsen method for 1 ns. Then, the production run was carried out in the NPT ensemble at 300 K with the time step of 1 fs. The temperature of the system was controlled by a V-rescale thermostat (τ_T = 1 ps), and the pressure was controlled by the Parrinello-Rahman method (τ_P = 2 ps). After 20 ns of simulation, the distributions of the particles were analyzed by the toolkits of GROMACS.

DFT calculation: all the calculations are performed in the framework of the DFT with the projector augmented plane-wave method, as implemented in the Vienna *ab initio* simulation package.[45] The generalized gradient approximation proposed by Perdew, Burke, and Ernzerhof is selected for the exchange-correlation potential.[46] The long range van der Waals interaction is described by the DFT-D3 approach.[43] The cut-off energy for plane wave is set to 500 eV. The energy criterion is set to 10^{-6} eV in iterative solution of the Kohn-Sham equation. A vacuum layer of 15 Å is added perpendicular to the sheet to avoid artificial interaction between periodic images. The K-mesh resolved in real space is 0.04 2π $Å^{-1}$. All the structures are relaxed until the residual forces on the atoms have declined to less than 0.03 eV $Å^{-1}$.

RESOURCE AVAILABILITY

Lead contact

Further information and requests for resources and reagents should be directed to and will be fulfilled by the lead contact, Hong Jin Fan (fanhj@ntu.edu.sg).

Materials availability

All reagents in this study are commercially available or can be easily prepared as indicated.

Data and code availability

There is no dataset or code associated with the paper.

ACKNOWLEDGMENTS

This research is supported by the National Research Foundation, Singapore, under its Singapore-China Joint Flagship Project (Clean Energy), and Ministry

of Education, Singapore, by AcRF Tier 2 (MOE-T2EP50121-0006). We thank BASF Shanshan Battery Materials Co. Ltd. for providing the LCO and LMO materials.

AUTHOR CONTRIBUTIONS

T.X. and J.-L.Y. conceived the concept of this research and completed the experimental design and execution. T.X., J.-L.Y., and H.J.F. co-wrote the manuscript. T.L. and Y.Z. provided the samples of VG. W.S.L. and L.L. completed the fabrication of Ag-VG. H.L., D.C., and H.B. provided assistance in spectroscopic characterization. H.J.F. supervised and guided this work. All authors participated in the analysis of the results and revision of the manuscript.

DECLARATION OF INTERESTS

The authors declare no competing interests.

SUPPLEMENTAL INFORMATION

Supplemental information can be found online at https://doi.org/10.1016/j.joule.2025.101820.

Received: November 6, 2024
Revised: December 17, 2024
Accepted: January 2, 2025
Published: January 31, 2025

REFERENCES

1. Bi, S.S., Wang, S., Yue, F., Tie, Z.W., and Niu, Z.Q. (2021). A rechargeable aqueous manganese-ion battery based on intercalation chemistry. Nat. Commun. *12*, 6991. https://doi.org/10.1038/s41467-021-27313-5.
2. Wu, X.Y., Markir, A., Xu, Y.K., Zhang, C., Leonard, D.P., Shin, W., and Ji, X.L. (2019). A rechargeable battery with an iron metal anode. Adv. Funct. Mater. *29*, 1900911. https://doi.org/10.1002/adfm.201900911.
3. Chang, S.Y., Gomez, J.F.F., Katiyar, S., Morell, G., and Wu, X.Y. (2023). Trivalent indium metal as a high-capacity, high-efficiency, low-polarization, and long-cycling anode for aqueous batteries. J. Am. Chem. Soc. *145*, 24746–24754. https://doi.org/10.1021/jacs.3c08677.
4. Yan, C.S., Lv, C., Wang, L.G., Cui, W., Zhang, L.Y., Dinh, K.N., Tan, H.T., Wu, C., Wu, T.P., Ren, Y., et al. (2020). Architecting a stable high-energy aqueous Al-ion battery. J. Am. Chem. Soc. *142*, 15295–15304. https://doi.org/10.1021/jacs.0c05054.
5. Zeng, Y.X., Lin, Z.Q., Meng, Y., Wang, Y.C., Yu, M.H., Lu, X.H., and Tong, Y.X. (2016). Flexible ultrafast aqueous rechargeable Ni//Bi battery based on highly durable single-crystalline bismuth nanostructured anode. Adv. Mater. *28*, 9188–9195. https://doi.org/10.1002/adma.201603304.
6. Zhang, H.Z., Liu, Q.Y., Zheng, D.Z., Yang, F., Liu, X.Q., and Lu, X.H. (2021). Oxygen-rich interface enables reversible stibium stripping/plating chemistry in aqueous alkaline batteries. Nat. Commun. *12*, 14. https://doi.org/10.1038/s41467-020-20170-8.
7. Katiyar, S., Chang, S.Y., Ullah, I., Hou, W.T., Conde-Delmoral, A., Qiu, S., Morell, G., and Wu, X.Y. (2024). Unlocking the potential of cadmium plating chemistry for low-polarization, long-cycling, and ultrahigh-efficiency aqueous metal batteries. Energy Environ. Sci. *17*, 4770–4779. https://doi.org/10.1039/d4ee01615g.
8. Zhou, W., Song, M., Liang, P., Li, X., Liu, X., Li, H., Zhang, T., Wang, B., Zhao, R., Zhao, Z., et al. (2023). High-energy Sn-Ni and Sn-air aqueous batteries via stannite-ion electrochemistry. J. Am. Chem. Soc. *145*, 10880–10889. https://doi.org/10.1021/jacs.3c03039.
9. Mondal, S., Choutipalli, V.S.K., Jena, B.K., Subramanian, V., and Raj, C.R. (2020). Bifunctional electrocatalytic activity of ordered intermetallics based on Pd and Sn. Journal. J. Phys. Chem. C *124*, 9631–9643. https://doi.org/10.1021/acs.jpcc.9b10417.
10. Tran, R., Xu, Z.H., Radhakrishnan, B., Winston, D., Sun, W.H., Persson, K.A., and Ong, S.P. (2016). Surface energies of elemental crystals. Sci. Data *3*, 160080. https://doi.org/10.1038/sdata.2016.80.
11. Mehl, M.J., Hicks, D., Toher, C., Levy, O., Hanson, R.M., Hart, G., and Curtarolo, S. (2017). The AFLOW Library of Crystallographic Prototypes: Part 1. Comp. Mater. Sci. *136*, S1–S828. https://doi.org/10.1016/j.commatsci.2017.01.017.
12. Yao, Y.X., Wang, Z.Y., Li, Z.J., and Lu, Y.C. (2021). A dendrite-free tin anode for high-energy aqueous redox flow batteries. Adv. Mater. *33*, e2008095. https://doi.org/10.1002/adma.202008095.
13. Chang, J.H., and Bard, A.J. (2014). Detection of the Sn(III) intermediate and the mechanism of the Sn(IV)/Sn(II) electroreduction reaction in bromide media by cyclic voltammetry and scanning electrochemical microscopy. J. Am. Chem. Soc. *136*, 311–320. https://doi.org/10.1021/ja409958a.
14. Yu, Z.H., Wang, Q., Li, Y.T., Zhang, F.Y., Ma, X.H., Zhang, X., Wang, Y.G., Huang, J.H., and Xia, Y.Y. (2024). Highly reversible tin redox chemistry for stable anode-free acidic proton battery. Joule *8*, 1063–1079. https://doi.org/10.1016/j.joule.2024.03.007.
15. Xu, D.Y., Zhang, H.Z., Xie, J.H., Zhou, L.J., Yang, F., Ma, J.F., Yu, Y.X., Wang, G.Z., and Lu, X.H. (2024). Highly reversible tin film anode guided via interfacial coordination effect for high energy aqueous acidic batteries. Adv. Mater. *36*, e2408067. https://doi.org/10.1002/adma.202408067.
16. Ouyang, J.X., Wang, Y.M., Wu, N., Wang, G.W., Xiao, L., Lu, J.T., and Zhuang, L. (2020). Dendrite-free Sn anode with high reversibility for aqueous batteries enabled by "water-in-salt" electrolyte. ACS Appl. Energy Mater. *3*, 5031–5038. https://doi.org/10.1021/acsaem.0c00557.
17. Zhang, H.Z., Xu, D.Y., Yang, F., Xie, J.H., Liu, Q.Y., Liu, D.J., Zhang, M.H., Lu, X.H., and Meng, Y.S. (2023). A high-capacity Sn metal anode for aqueous acidic batteries. Joule *7*, 971–985. https://doi.org/10.1016/j.joule.2023.04.011.
18. Xu, D.Y., Xie, J.H., Zhou, L.J., Yang, F., Wang, Y., Yang, Z.J., Wang, F.X., Zhang, H.Z., and Lu, X.H. (2023). Tendency regulation of competing reactions toward highly reversible tin anode for aqueous alkaline batteries. Small *19*, e2301931. https://doi.org/10.1002/smll.202301931.
19. Chang, S., Hou, W., Del Valle-Perez, A., Ullah, I., Qiu, S., Rodriguez, J.L., Díaz-Vázquez, L.M., Cunci, L., Morell, G., and Wu, X. (2024). A low-acidity chloride electrolyte enables exceptional reversibility and stability in aqueous tin metal batteries. Angew. Chem. Int. Ed. Engl. e202414346. https://doi.org/10.1002/anie.202414346.
20. Mu, Y.B., Li, Z., Wu, B.K., Huang, H.D., Wu, F.H., Chu, Y.Q., Zou, L.F., Yang, M., He, J.F., Ye, L., et al. (2023). 3D hierarchical graphene matrices enable stable Zn anodes for aqueous Zn batteries. Nat. Commun. *14*, 4205. https://doi.org/10.1038/s41467-023-39947-8.
21. Jiao, Q.Y., Zhai, X.W., Sun, Z.X., Wang, W.J., Liu, S.H., Ding, H., Chu, W.S., Zhou, M., and Wu, C.Z. (2023). Ultrafast superfilling construction of a metal artificial interface for long-term stable zinc anodes. Adv. Mater. *35*, e2300850. https://doi.org/10.1002/adma.202300850.
22. Zeng, Y.X., Pei, Z.H., Luan, D.Y., and Lou, X.W.D. (2023). Atomically dispersed zincophilic sites in N,P-codoped carbon macroporous fibers enable efficient Zn metal anodes. J. Am. Chem. Soc. *145*, 12333–12341. https://doi.org/10.1021/jacs.3c03030.
23. Xu, K., Zheng, X.H., Luo, R.H., Sun, J.F., Ma, Y.R., Chen, N., Wang, M.M., Song, L., Zhao, Q.B., and Chen, W. (2023). A three-dimensional zincophilic nano-copper host enables dendrite-free and anode-free Zn batteries. Mater. Today Energy *34*, 101284. https://doi.org/10.1016/j.mtener.2023.101284.
24. Scharifker, B., and Hills, G. (1983). Theroretical and experimental studies of multiple nucleaion. Electrochim. Acta *28*, 879–889. https://doi.org/10.1016/0013-4686(83)85163-9.
25. Tylka, M.M., Willit, J.L., and Williamson, M.A. (2017). Electrochemical nucleation and growth of uranium and plutonium from molten salts.

J. Electrochem. Soc. *164*, H5327–H5335. https://doi.org/10.1149/2.0471708jes.

26. Zou, Q.L., Liang, Z.J., Wang, W.W., Dong, D.J., and Lu, Y.C. (2023). A nuclei-rich strategy for highly reversible dendrite-free zinc metal anodes. Energy Environ. Sci. *16*, 6026–6034. https://doi.org/10.1039/d3ee03246a.
27. Bi, J.X., Liu, Y.H., Du, Z.Z., Wang, K., Guan, W.Q., Wu, H.W., Ai, W., and Huang, W. (2024). Bottom-up magnesium deposition induced by paper-based triple-gradient scaffolds toward flexible magnesium metal batteries. Adv. Mater. *36*, e2309339. https://doi.org/10.1002/adma.202309339.
28. Lin, D.W., Shi, D.H., Zhu, A.Q., Yang, C.K., Zhang, T., Liu, K., Liu, K.L., Hong, G., and Zhang, W.J. (2024). Self-adaptive hierarchical hosts with switchable repulsive shielding for dendrite-free zinc-ion batteries. Adv. Energy Mater. *14*, 2304535. https://doi.org/10.1002/aenm.202304535.
29. Xi, M.R., Liu, Z.J., Wang, W., Qi, Z.H., Sheng, R., Ding, J., Huang, Y.D., and Guo, Z.P. (2024). Shear-flow induced alignment of graphene enables the closest packing crystallography of the (002) textured zinc metal anode with high reversibility. Energy Environ. Sci. *17*, 3168–3178. https://doi.org/10.1039/d3ee04360f.
30. Zheng, Y.Q., Sun, P.X., Zhang, X.Y., Li, N.W., Wu, L.L., Luan, D.Y., Zhang, X.T., Lou, X.W.D., and Yu, L. (2024). Decoration of Ag species into reduced graphene oxide foam as a superelastic and robust host toward stable Zn metal anodes under dwell-fatigue condition. Adv. Mater. *36*, e2405906. https://doi.org/10.1002/adma.202405906.
31. Wang, G.X., Liu, X., Shi, H.C., Ma, Y.L., Wang, Z.C., Sun, C.H., Song, F.C., Zhang, Z.H., Dong, S.M., Sun, M.L., et al. (2024). Achieving planar electroplating/stripping behavior of magnesium metal anode for a practical magnesium battery. ACS Energy Lett. *9*, 48–55. https://doi.org/10.1021/acsenergylett.3c02058.
32. Chai, X., Xie, H.H., Zhang, T.T., Xin, Y., Zhang, F., He, B.J., Xie, H.K., Yu, L., and Tian, H.J. (2024). Ternary Mg alloy-based artificial interphase enables high-performance rechargeable magnesium batteries. Energy Storage Mater. *70*, 103460. https://doi.org/10.1016/j.ensm.2024.103460.
33. Wang, S.X., Guo, Y., Du, X.F., Xiong, L.L., Liang, Z.S., Ma, M.B., Xie, Y.H., You, W.Z., Meng, Y., Liu, Y.F., and Liu, M.X. (2024). Preferred crystal plane electrodeposition of aluminum anode with high lattice-matching for long-life aluminum batteries6476. Nat. Commun. *15*, 6476. https://doi.org/10.1038/s41467-024-50723-0.
34. Yan, C.S., Lv, C.D., Jia, B.E., Zhong, L.X., Cao, X., Guo, X.L., Liu, H.J., Xu, W.J., Liu, D.B., Yang, L., et al. (2022). Reversible Al metal anodes enabled by amorphization for aqueous aluminum batteries. J. Am. Chem. Soc. *144*, 11444–11455. https://doi.org/10.1021/jacs.2c04820.
35. Vasileff, A., Zhi, X., Xu, C.C., Ge, L., Jiao, Y., Zheng, Y., and Qiao, S.Z. (2019). Selectivity control for electrochemical CO_2 reduction by charge redistribution on the surface of copper alloys. ACS Catal. *9*, 9411–9417. https://doi.org/10.1021/acscatal.9b02312.
36. Jiang, X.X., Wang, X.K., Liu, Z.J., Wang, Q.L., Xiao, X., Pan, H.P., Li, M., Wang, J.W., Shao, Y., Peng, Z.Q., et al. (2019). A highly selective tin-copper bimetallic electrocatalyst for the electrochemical reduction of aqueous CO_2 to formate. Appl. Cat. B *259*, 118040. https://doi.org/10.1016/j.apcatb.2019.118040.
37. Mann, J.B., Meek, T.L., Knight, E.T., Capitani, J.F., and Allen, L.C. (2000). Configuration energies of the d-block elements. J. Am. Chem. Soc. *122*, 5132–5137. https://doi.org/10.1021/ja9928677.
38. Xiao, T., Yang, J.L., Zhang, B., Wu, J.W., Li, J.L., Mai, W.J., and Fan, H.J. (2024). All-round ionic liquids for shuttle-free zinc-iodine battery. Angew. Chem. Int. Ed. Engl. *63*, e202318470. https://doi.org/10.1002/anie.202318470.
39. Chen, S.M., Ying, Y.R., Wang, S.N., Ma, L.T., Huang, H.T., Wang, X.Q., Jin, X., Bai, S.C., and Zhi, C.Y. (2023). Solid interhalogen compounds with effective Br^0 fixing for stable high-energy zinc batteries. Angew. Chem. Int. Ed. Engl. *62*, e202301467. https://doi.org/10.1002/anie.202301467.
40. Van der Spoel, D., Lindahl, E., Hess, B., Groenhof, G., Mark, A.E., and Berendsen, H.J.C. (2005). GROMACS: Fast, flexible, and free. J. Comp. Chem. *26*, 1701–1718. https://doi.org/10.1002/jcc.20291.
41. Berendsen, H.J.C., van der Spoel, D., and van Drunen, R. (1995). GROMACS - A message-passing parallel molecular-dynamics implementation. Comput. Phys. Commun. *91*, 43–56. https://doi.org/10.1016/0010-4655(95)00042-e.
42. Martínez, L., Andrade, R., Birgin, E.G., and Martínez, J.M. (2009). PACKMOL: A package for building initial configurations for molecular dynamics simulations. J. Comp. Chem. *30*, 2157–2164. https://doi.org/10.1002/jcc.21224.
43. Grimme, S., Antony, J., Ehrlich, S., and Krieg, H. (2010). A consistent and accurate ab initio parametrization of density functional dispersion correction (DFT-D) for the 94 elements H-Pu. J. Chem. Phys. *132*, 154104. https://doi.org/10.1063/1.3382344.
44. Lu, T., and Chen, F.W. (2012). Multiwfn: A multifunctional wavefunction analyzer. J. Comp. Chem. *33*, 580–592. https://doi.org/10.1002/jcc.22885.
45. Kresse, G., and Joubert, D. (1999). From ultrasoft pseudopotentials to the projector augmented-wave method. Phys. Rev. B *59*, 1758–1775. https://doi.org/10.1103/PhysRevB.59.1758.
46. Perdew, J.P., Burke, K., and Ernzerhof, M. (1996). Generalized gradient approximation made simple. Phys. Rev. Lett. *77*, 3865–3868. https://doi.org/10.1103/PhysRevLett.77.3865.